Minimum Quantum Run-Time Characterization and Calibration via Restless Measurements with Dynamic Repetition Rates

Caroline Tornow[1,2] Naoki Kanazawa[3] William E. Shanks[4] and Daniel J. Egger[2,*]

[1]*ETH Zurich, 8093, Switzerland*
[2]*IBM Quantum – IBM Research - Zurich, Säumerstrasse 4, Rüschlikon 8803, Switzerland*
[3]*IBM Quantum – IBM Research Tokyo, Tokyo, 103-8510, Japan*
[4]*IBM Quantum – IBM T.J. Watson Research Center, Yorktown Heights, New York 10598, USA*

The performance of a quantum processor depends on the characteristics of the device and the quality of the control pulses. Characterizing cloud-based quantum computers and calibrating the pulses that control them is necessary for high-fidelity operations. However, this time-intensive task eats into the availability of the device. Here, we show restless measurements with a dynamic repetition rate that speed-up calibration and characterization tasks. Randomized benchmarking is performed 5.3 times faster on the quantum device than when an active reset is used and without discarding any data. In addition, we calibrate a qubit with parameter scans and error-amplifying gate sequences and show speed-ups of up to a factor of 40 on the quantum device over active reset. Finally, we present a methodology to perform restless quantum process tomography that mitigates restless state preparation errors. These results reduce the footprint of characterization and calibration tasks. Quantum computers can thus either spend more time running applications or run calibrations more often to maintain gate fidelity.

I. INTRODUCTION

Quantum computers have the potential to impact a wide range of applications [1–6]. Their performance is measurable along three dimensions, quality, scale, and speed [7]. Quantum volume [8,9], for example, measures scale and quality. However, maintaining the quality of a quantum computer requires periodic gate calibration and characterization performed by jobs interleaved with normal circuit execution. These jobs therefore take up time on the quantum processor. Reducing the time they take increases system availability and enables more frequent calibration, thus resulting in higher quality.

High-quality gates require carefully designed pulse shapes, such as derivative removal by adiabatic gate (DRAG) [10], calibrated to the quantum system. Analytic pulses with few parameters are typically calibrated using gate sequences tailored to amplify different errors such as over or under rotations and phase errors [11]. Quantum optimal control [12] provides methods to design

gates [13–15], reduce pulse duration [16–18], and increase fidelity [19]. However, to overcome drifts and model inaccuracies, these methods often require data-intensive closed-loop optimization [18–20]. This makes fewer control parameters [21] and high-speed data acquisition desirable [22,23]. Optimal control requires a fidelity metric to optimize. Randomized benchmarking (RB) measures the average gate fidelity [24–26] and provides a state preparation and measurement (SPAM) error insensitive metric to both optimize quantum gates [18,19,22] and learn the underlying system model [27]. By contrast, quantum process tomography (QPT) measures the gate fidelity [28–34] and provides more information on the process matrix but is sensitive to SPAM errors. Combining RB with quantum process tomography improves model learning [27].

Speed is influenced by both classical and quantum elements [7] such as run-time compilation and the ability to quickly reset the qubits. Superconducting qubit-based quantum processors [35–37] enjoy long coherence times [38,39] and comparatively short gates. Long T_1 times make active reset necessary since waiting 5 to 10 times T_1 is inefficient [7]; see Fig. 1(a). However, active reset also requires time and typically lasts a few microseconds [40–45]. For example, the qubits can be unconditionally reset by applying a π pulse to the $|1\rangle$ to $|2\rangle$ transition of the transmon and then driving the transition between the $|2\rangle$ state of the transmon and the first excited state of the
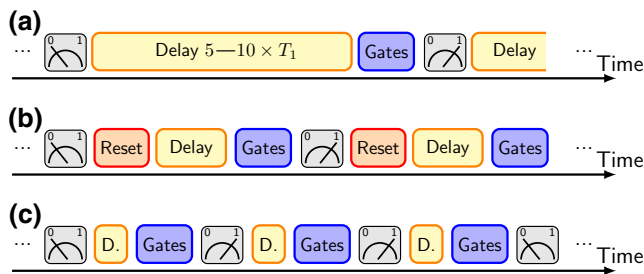
*deg@zurich.ibm.com

FIG. 1. Illustration of qubit initialization schemes. Time axes are not to scale. (a) The qubit is passively reset to the ground state by waiting 5 to 10 times the T_1 time. (b) The qubit is actively reset after each measurement. A 50 to 250 μs delay is often necessary to ensure a high reset quality. (c) Restless measurements where the outcome of the previous measurement initializes the qubit to either $|0\rangle$ or $|1\rangle$. A short delay of typically 1 μs is sometimes needed to allow time for classical processing of the readout signal.

readout resonator where the excitation quickly decays to the environment [43,44]. Furthermore, a delay is often necessary after a reset operation to avoid deteriorating the initialization quality [44]; see Fig. 1(b). For example, on IBM Quantum systems this configurable delay currently has a default value of 50 to 250 μs depending on the system [7]. In restless measurements the qubits are not reset in between circuits. This provides a fast alternative to several characterization and calibration tasks [18,22,23]. Here, the outcome of the projective measurement at the end of a circuit initializes the qubits to either $|0\rangle$ or $|1\rangle$ for the next circuit; see Fig. 1(c). For a large class of circuits, the states 0 and 1 can be relabeled without modifying the circuit.

Quantum circuits can either be executed with a static or a dynamic repetition rate. With a static repetition rate R, each circuit must fit within the period $1/R$. By contrast, when the repetition rate is dynamic, a quantum circuit will begin executing a fixed delay after the previous circuit completed. Here, we demonstrate that a dynamic repetition rate improves the quality of restless measurements. Indeed, restless measurements with a static repetition rate R must fit all gates and readout operations for each circuit within a period $1/R$ [23]. This produces a variable delay after each measurement when the circuits have a different duration as in RB and therefore a variable state preparation error. By contrast, when the repetition rate is dynamic, there is a short fixed delay after each circuit and consequently a fixed state preparation error. In Sec. II we review restless measurements. Next, in Sec. III, we show that, by using dynamic repetition rates, all of the restless randomized benchmarking data are usable, as opposed to discarding 60% of the data as in Ref. [23]. In Sec. IV, we show restless qubit calibration with error amplifying gate sequences. Furthermore, we show in Sec. V how to perform QPT with restless measurements and how to mitigate state preparation errors. We conclude in Sec. VI.

II. RESTLESS MEASUREMENTS

IBM Quantum systems are built with fixed-frequency transmon qubits dispersively coupled to readout resonators. The N measurement shots of K circuits are gathered by sequentially measuring each circuit and repeating this N times. By default, these systems reset the qubits to their ground state and introduce a fixed delay after each measurement. This reset can be turned off and the delay reduced from 250 μs to a microsecond or less to perform restless measurements with a dynamic repetition rate; see the details in Appendix A. Now, if a qubit is measured in state $|i\rangle$ for circuit $k-1$ with $i \in \{0, 1\}$ then the initial state of the next circuit k is also $|i\rangle$. Therefore, the measured outcomes of restless experiments require postprocessing.

A. Restless data postprocessing

Each qubit is measured by digitizing and then integrating a measurement pulse transmitted through the readout resonator. Each shot therefore results in a single complex number represented as an in-phase and quadrature (IQ) component in the IQ plane. These IQ points are discriminated into $|0\rangle$ or $|1\rangle$ states when a trained discriminator is available [46]. By default, running K circuits with N shots and n qubits on an IBM Quantum system returns K count dictionaries $\{i : C_{i,k}\}_k$. Here, the count $C_{i,k}$ with $i \in \{0, 1\}^n$ is the number of times state $|i\rangle$ is measured for circuit $k = 1, \ldots, K$. Furthermore, the counts sum to the total number of shots, e.g., $C_{00,k} + C_{01,k} + C_{10,k} + C_{11,k} = N$ when $n = 2$.

These count dictionaries are unusable in restless measurements. Instead, to postprocess restless data, we require the measurement outcome of each shot that the backends can return as a list of outcomes grouped by circuit called the *memory*; see Fig. 2. The state before the very first circuit is typically $|0\rangle$. The execution begins and each restless single-qubit measurement generates a bit that is appended to the memory of its corresponding circuit; see Fig. 2(a). The memory is postprocessed in three steps; see Fig. 2(b). First, the bits are sorted according to the order in which they are acquired. We label these time-ordered bits m_j with $m_{-1} = 0$ to represent the ground state before the first circuit. Next, we reclassify each bit with the exclusive OR operation to identify state changes, i.e., $m'_j = m_{j-1} \oplus m_j$. Measurements for which the state changed are identified as the 1 state and those with no change as the 0 state. These new classified states are then analyzed as normal by building count dictionaries. This process can be generalized to certain multiqubit cases by analyzing the outcome of each qubit independently of the others.

Previous work required additional postprocessing to account for qubit decay [23]. However, in this work, because of improved qubit lifetimes and reduced delay times, the error due to qubit decay is negligible compared to readout errors and so no additional correction is
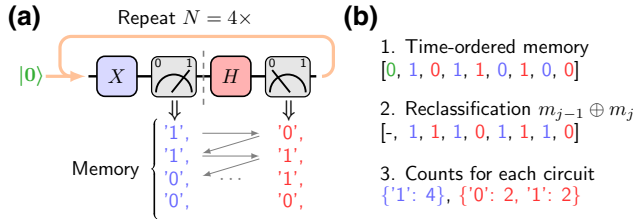
FIG. 2. Illustration of the restless data postprocessing of a single-qubit job with two circuits and four shots. (a) The qubit begins in a known state, typically $|0\rangle$. The first circuit is an X gate followed by a measurement and the second circuit is a Hadamard gate followed by a measurement. The delays are not shown. The measurement outcomes are color coded according to the circuit that generated them. (b) The measurement outcomes are time ordered, reclassified with XOR, and summed into count dictionaries.

needed. Furthermore, such errors are typically absorbed by fit parameters in RB and calibration experiments.

B. Speed-up

We compare each restless experiment to a standard one with active qubit reset and interleave standard and restless jobs to avoid biases due to eventual drifts. In particular, we compare the time spent by the quantum processor executing the quantum circuits in both settings. This time is given by

$$\tau^{(x)} = NK(\tau_{\text{reset}}^{(x)} + \tau_{\text{delay}}^{(x)} + \langle\tau_{\text{circ}}\rangle + \tau_{\text{meas}}), \quad (1)$$

where $\tau_{\text{reset}}^{(x)}$ and $\tau_{\text{delay}}^{(x)}$ are the reset and delay times, respectively. Here, the measurement time τ_{meas} includes the measurement pulse and a short delay of typically $10/(2\pi\kappa)$ that allows the resonator to depopulate where κ is the resonator linewidth. The superscript (x) indicates restless (r) or standard (s) measurements. The average duration of all K circuits in an experiment is $\langle\tau_{\text{circ}}\rangle = K^{-1}\sum_{k=1}^{K}\tau_{\text{circ},k}$, where $\tau_{\text{circ},k}$ is the duration of only the gates in circuit k. We therefore compute the quantum processor speed-up of restless measurements as $\tau^{(s)}/\tau^{(r)}$, which is independent of the number of circuits and shots due to Eq. (1). In the terminology of Ref. [7], this speed-up considers the circuit delay and circuit execution times but not the run-time compilation and data transfer times.

III. RANDOMIZED BENCHMARKING

In standard RB the probability of the ground state P_0 is measured after a sequence of N_c Clifford gates that compose to the identity. Fitting P_0 to $A\alpha^{N_c} + B$, where A, B, and α are fit parameters, yields the average error per Clifford gate (EPC) as $(1 - \alpha)/2$ and $3(1 - \alpha)/4$ for single- and two-qubit RB, respectively. Restless RB measurements with a fixed trigger rate R only reproduce the

average gate fidelity if the outcomes where a qubit began in the excited state are discarded [23]. This is because the variable length of the Clifford sequences creates a variable delay when $1/R$ is constant. The consequence is a state preparation error dependent on the number of Clifford gates; see Fig. 3(a). Therefore, 60% of the restless data in Ref. [23] was discarded, lowering the effective restless repetition rate by a factor of 2.5. With a dynamic repetition rate we no longer need to discard data. Now, each Clifford sequence begins after the previous one with the same delay; all Clifford sequences therefore have the same state preparation error—see Fig. 3(b).

We compare standard and restless RB using Qiskit Experiments [47] and the data processor described in Sec. II A. We measure 11 and 14 sequences of Clifford gates with N_c ranging from 1 to 5101 and from 1 to 196 for single- and two-qubit RB, respectively. Each length N_c is measured for ten different random realizations with $N = 1024$ shots. In restless RB there is a fixed 1 μs delay after each measurement. Single-qubit RB is done on qubit 13 of *ibmq_sydney*. We measure an EPC of $0.035\% \pm 0.001\%$ and $0.035\% \pm 0.001\%$ for three independent standard and restless RB experiments, respectively; see Fig. 3(c) and Appendix B. Two-qubit RB is done on qubits 8 and 11 of *ibmq_sydney* for which we measure an EPC of $1.703\% \pm 0.031\%$ and $1.780\% \pm 0.037\%$ for three independent standard and restless RB experiments, respectively; see Fig. 3(d). We observe a lower A coefficient of the restless RB curves with respect to the standard one; see Figs. 3(c)–3(d) and Appendix B. We attribute this scaling to T_1-induced state preparation errors in the restless measurements that reduce the probability that the qubit measured in $|1\rangle$ will also be measured in $|1\rangle$ after the subsequent Clifford sequence. Crucially, this state preparation error does not significantly affect the measured depolarizing parameter α. To further illustrate this, we split the single-qubit restless RB shots into two sets depending on the initial state of the qubit and analyze each set independently. The data with the qubit in $|0\rangle$ have an A value of 0.485(5), i.e., almost identical to the 0.487(3) produced by the standard measurement, while the data with the qubit in $|1\rangle$, shown in Fig. 3(c), have an A of 0.426(3). Finally, to demonstrate the importance of the restless data processor, we process the restless data with the standard data processing chain. This results in the useless green curves in Figs. 3(c) and 3(d).

We compute the restless speed-up with Eq. (1). Our schedules have a $\langle\tau_{\text{circ}}\rangle$ of 55.87 and 51.81 μs for single- and two-qubit RB, respectively. Restless measurements therefore result in a 5.1 and 5.3 times speed-up over standard measurements on *ibmq_sydney* for single- and two-qubit RB, respectively; see Table I. On systems such as *ibmq_montreal* that have a 50 μs delay these speed-ups become 1.9 and 1.7 times, which emphasises the impact of the delay [7]. We show RB data in Appendix B taken

TABLE I. Run-time breakdown on the quantum processor of RB with 11 and 14 different lengths of ten random Clifford gate sequences at each length for the one- and two-qubit experiments, respectively, with $N = 1024$ shots. Therefore, $KN = 10 \times 11 \times 1024$ and $KN = 10 \times 14 \times 1024$.

Processor (restless)	τ_{meas} (μs)	τ_{reset}[a] (μs)	τ_{delay} (μs)	$\langle\tau_{\text{circ}}\rangle$ (μs)	$\tau^{(x)}$ (s)
		Single qubit			
ibmq_sydney (✗)	5.4	4	250.0	55.87	35.51
ibmq_sydney (✓)	5.4	n.m.	1.0	55.87	7.01
ibmq_montreal (✗)	5.2	4	50.0	55.87	12.96
ibmq_montreal (✓)	5.2	n.m.	0.5	55.87	6.93
		Two qubits			
ibmq_sydney (✗)	5.4	4	250.0	51.81	44.61
ibmq_sydney (✓)	5.4	n.m.	1.0	51.81	8.34
ibmq_montreal (✗)	5.2	4	50.0	65.64	17.90
ibmq_montreal (✓)	5.2	n.m.	0.5	65.64	10.23

[a]We assume $4\,\mu$s since the backends do not disclose the exact duration of the reset, which is typically between 3 and 5 μs; "n.m." stands for "not meaningful".

DRAG pulses whose pulse envelope is $\Omega_x(t) + i\beta\partial_t\Omega_x(t)$. Here, Ω_x is a Gaussian pulse envelope with amplitude A measured as a fraction of the maximum output of the arbitrary waveform generator, and β is the DRAG parameter [10].
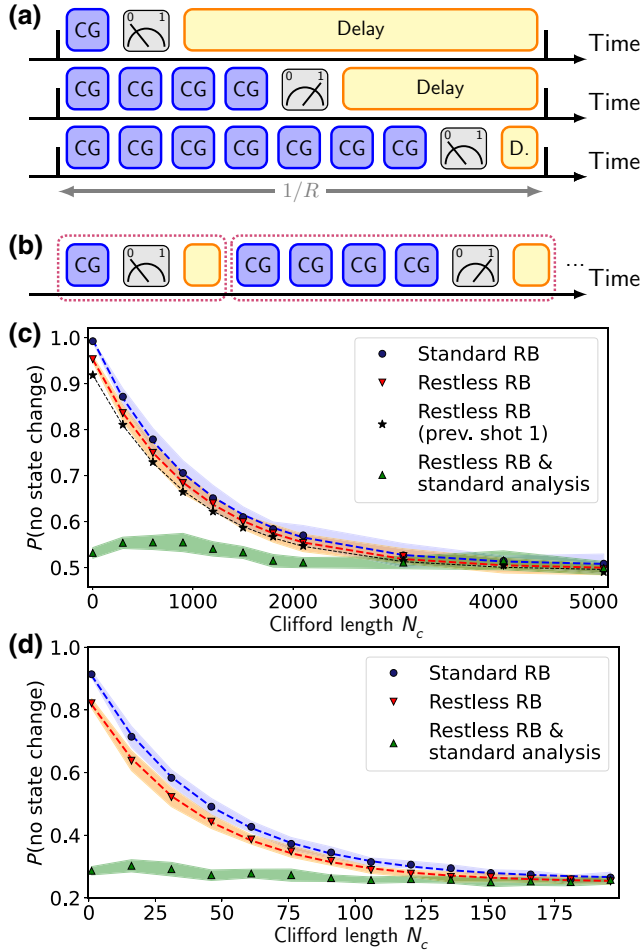
FIG. 3. Standard and restless RB. (a) With a fixed rate (thick black ticks), there is a variable delay that depends on the number of Clifford gates (CG) (blue squares). (b) With a dynamic repetition rate, the delay after each measurement is identical for each circuit. (c) Single-qubit and (d) two-qubit standard (blue circles) and restless RB (red triangles) with dynamic repetition rates. The green triangles show restless data analyzed with the standard data processor. The markers are the mean values of ten random realizations of Clifford sequences and the shaded areas are the standard deviation. The dotted line with star markers in (c) shows restless RB postselected to include only the data for which the qubit begins in state $|1\rangle$.

on *ibmq_montreal* for different RB circuits. The T_1 and T_2 times and readout errors of all used qubits can be found in Table IV in Appendix C.

IV. CALIBRATION

Calibration experiments determine the parameters of the control pulses to ensure quality. Typically, different experiments are run where each is dedicated to measure a single parameter. Here, we show a restless calibration workflow built on the data processor of Sec. II A. We run the calibration experiments on different devices based on system availability. We illustrate restless calibration by calibrating

A. Parameter scans

Parameter scans give a first estimate of a parameter value. For example, the Rabi oscillation measured in Ref. [23] yields a rough estimation of the amplitude of Ω_x as a function of the target rotation angle. We now demonstrate a restless parameter scan to estimate β using the gate sequence $[R_z(\pi)X(\beta)R_z(\pi)X(\beta)]^n$. This sequence is repeated for different β values and $n \in \{3, 5, 7\}$. The virtual $R_z(\pi)$ rotations change the X gate from a π rotation to a $-\pi$ rotation [48]. Ideally, this gate sequence rotates between the poles of the Bloch sphere in the Y-Z plane and composes to the identity. However, as phase errors accumulate, due to the higher levels of the transmon, the state vector drifts out of the Y-Z plane and oscillations in the qubit population appear [49,50]. The measured population is fit to oscillating functions to estimate the β that minimizes errors. Standard and restless measurements on *ibmq_quito* both produce the same oscillating pattern with high-quality fits, as indicated by the low χ^2 values [see Figs. 4(a) and 4(b)], resulting in a β of -0.376 ± 0.006 and -0.355 ± 0.007, respectively, averaged over three independent measurements. As expected, applying the standard data processor to restless measurements yields a useless signal; see Fig. 4(c). Crucially, the restless speed-up obtained following Sec. II B is 38.4 times.
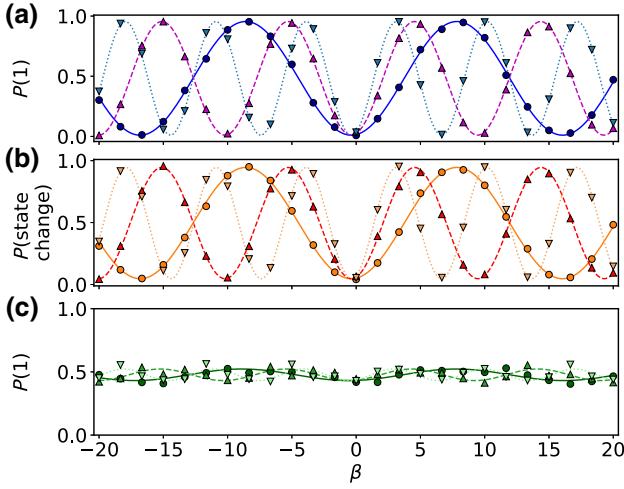
FIG. 4. Rough DRAG calibration of *ibmq_quito* qubit 1. The solid, dashed, and dotted lines represent $n = 3$, 5, and 7, respectively. (a) Standard measurements ($\chi^2 = 1.2$). (b) Restless measurements ($\chi^2 = 1.3$). (c) Restless measurements with the standard data processing.

B. Single-qubit error amplifying gate sequences

We now consider error amplifying gate sequences that repeat a gate pattern n times to amplify an error $d\theta$ to $nd\theta$. Typically, the measured qubit population P (or the state change probability in the restless case) is fit to

$$\frac{a}{2}\cos[n(\theta + d\theta) - \phi] + b. \quad (2)$$

Here, the intended angle per gate θ and the phase ϕ are fixed by the values of P for ideal gates. However, a, b, and $d\theta$ are fit parameters.

The pulse amplitude-error amplifying sequence of the $\sqrt{X}$ gate applies $\sqrt{X}$ an odd number of times. The ideal states lie on the equator of the Bloch sphere that maximizes the measurement's sensitivity to $d\theta$. The ideal gate sequence therefore imposes $\theta = \pi/2$ and $\phi = \pi$ in Eq. (2). Two calibration points, one without any gates and one with two $\sqrt{X}$ gates, allow us to accurately fit a in Eq. (2). To demonstrate restless amplitude calibration, we add an error dA to the amplitude A of the $\sqrt{X}$ gate reported by qubit 1 of *ibmq_jakarta* ranging from -5% to 5%. We interleave restless and standard jobs to mitigate biases due to drifts. We measure the resulting $d\theta$ by fitting the data obtained with both restless and standard measurements to Eq. (2). Both methods produce good fits, as indicated by the low χ^2 values; see Figs. 5(a) and 5(b). The fitted rotation errors $d\theta$ reproduce the expected deviation $d\theta_{\mathrm{exp}} = -(\pi/2)dA/(dA + A)$ and on average differ by 1.7 ± 0.9 mrad and -2.3 ± 1.3 mrad in the standard and restless cases, respectively; see Figs. 5(c) and 5(d). As reference, note that a 1 mrad rotation error corresponds to a gate error of 2.5×10^{-7} on an otherwise perfect $\sqrt{X}$
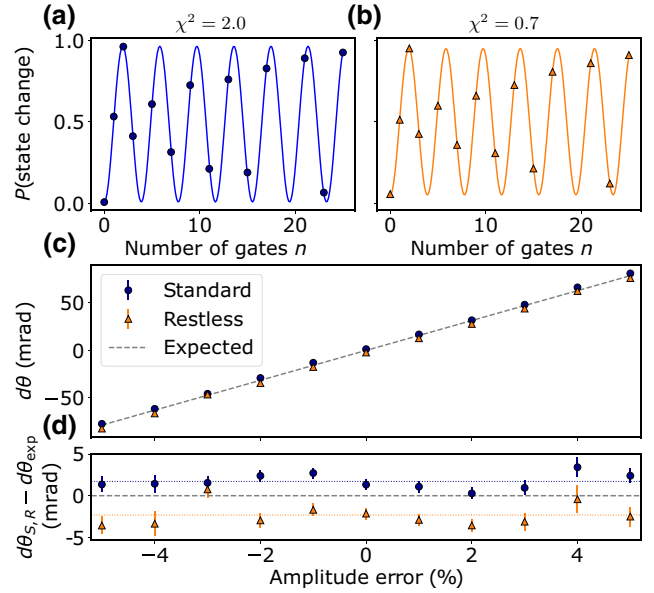

FIG. 5. Fine amplitude calibration of a $\sqrt{X}$ gate on *ibmq_jakarta* qubit 1. Qubit population as a function of the number of $\sqrt{X}$ gates for (a) standard and (b) restless measurements with a 3% amplitude error. (c) The measured deviation angle $d\theta$ as a function of the added amplitude error. The dashed gray line indicates the expected deviation $d\theta_{\mathrm{exp}}$. (d) Deviation from the expected values $d\theta_{\mathrm{exp}}$. The subscripts S and R indicate the standard and restless data, respectively.

gate. We compute the restless speed-up for one experiment with Eq. (1). With $\langle\tau_{\mathrm{circ}}\rangle = 0.39$ μs, a default repetition delay of 250 μs, and a restless repetition delay of 1 μs, we obtain $\tau^{(s)} = 3.724$ s and $\tau^{(r)} = 0.0973$ s and therefore a 38.3 times speed-up.

We now consider the DRAG-error amplifying sequence $\sqrt{X}R_z(-\pi/2)[R_z(\pi)\sqrt{X}R_z(\pi)\sqrt{X}]^n\sqrt{X}$. The first $\sqrt{X}$ rotation moves the state to the equator of the Bloch sphere. The sequence $R_z(\pi)\sqrt{X}R_z(\pi)\sqrt{X}$ causes the state to oscillate between the equator and the $|1\rangle$ state. The final $\sqrt{X}R_z(-\pi/2)$ gates map phase errors that took the state vector out of the Y-Z plane during the oscillation onto the Z axis for measurement. We add an error $d\beta$ ranging from -20% to 20% to the calibrated β value of the $\sqrt{X}$ gate reported by *ibmq_montreal* qubit 3. Next, we measure DRAG-error amplifying sequences in a restless and standard setting. The resulting data are fit to Eq. (2) with $\theta = 0$, $\phi = \pi/2$, and a fixed to 1 to measure $d\theta$. Once again, we observe good agreement between standard and restless measurements; see Fig. 6. For this experiment, the restless speed-up is 9.3 times since the default repetition delay of *ibmq_montreal* is 50 μs.

C. Two-qubit error amplifying gate sequences

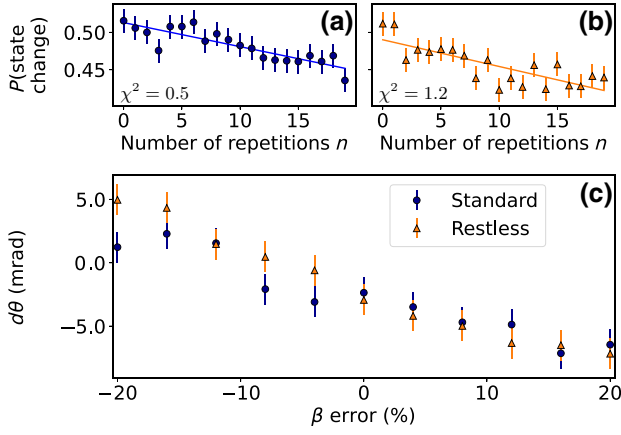We now consider error amplifying gate sequences to determine amplitude errors for the two-qubit

FIG. 6.   Characterization of β-induced errors on qubit 3 of *ibmq_montreal*. Qubit population as a function of the number of repetitions n for (a) standard and (b) restless measurements with a 20% DRAG parameter error. (c) The measured deviation angle $d\theta$ as a function of the added β error.

gate

$$R_{ZX}(\theta) = \begin{pmatrix} R_X(\theta) & 0 \\ 0 & R_X(-\theta) \end{pmatrix} \quad (3)$$

with restless measurements. With an angle of $\theta = \pi/2$, this gate is a perfect entangler and can create a controlled-NOT (CNOT) gate. Fixed-frequency transmons implement R_{ZX} with an echoed cross-resonance pulse sequence [51] augmented with rotary tones [52]. Amplitude errors are amplified and measured by repetitively applying $R_{ZX}(\pi/2)$; see Fig. 7(a). We compare standard and restless measurements by adding an amplitude error dA to the CR pulses of the

calibrated R_{ZX} pulse schedule reported by the backend; see Fig. 7(b). When the qubits are reset, only the target qubit needs to be measured, which results in the same pattern as for the single-qubit $\sqrt{X}$ gate; compare Fig. 5(a) with Fig. 7(c). However, for restless measurements, both qubits must be measured and some shots may project the control qubit, initially in the $|0\rangle$ state, into the $|1\rangle$ state. This changes the sign of the subsequent rotations of the target qubit. We account for this by computing the probability of a state change of the target qubit conditional on the control qubit. This results in two data sets, shown in Fig. 7(d), that exhibit the same pattern since an R_X rotation with an angle $\pm n(\theta + d\theta)$ results in the same qubit population when starting from the poles of the Bloch sphere. We fit the data to two functions: both are given by Eq. (2) and share the same $d\theta$ fit parameter. However, each function has its own a and b parameters to accommodate differences in signal amplitude that we attribute to T_1 and the imperfect readout of the control qubit. The restless measured $d\theta$ closely follow the standard measurements, albeit with a 8.3 ± 3.0 mrad bias that corresponds to a gate error of 1.7×10^{-5} on an otherwise perfect $R_{ZX}(\pi/2)$ gate, see Figs. 7(e) and 7(f). For this experiment, we obtain a restless speed-up of 28.8 times.

D. Calibration and characterization

We now tie Secs. III, IV A, and IV B together by calibrating and characterizing the $\sqrt{X}$ gate of *ibmq_bogota* qubit 2 with standard and restless measurements. We calibrate the amplitude A and DRAG parameter β and fix the duration and standard deviation of the Gaussian pulse to 160 and 40 samples, respectively. Each sample has a
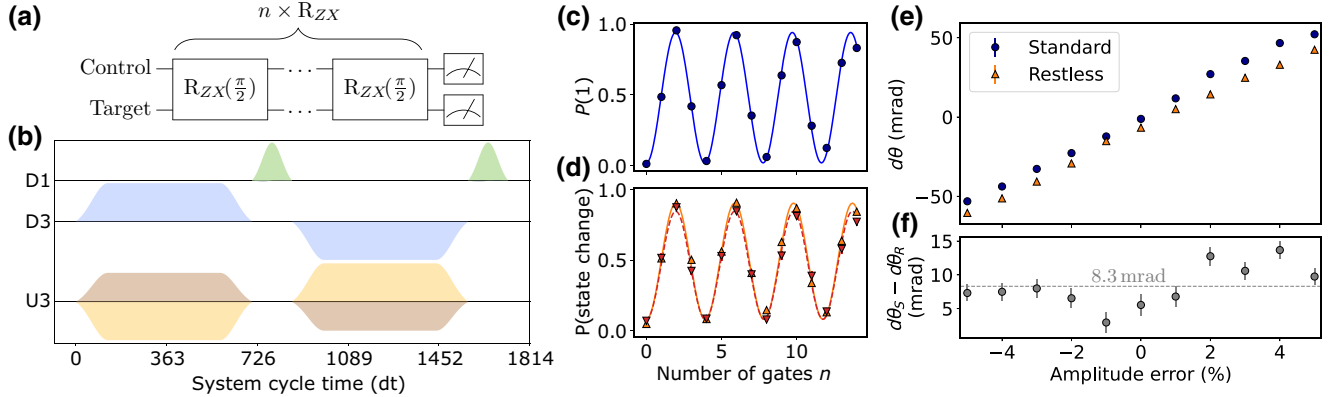

FIG. 7.   (a) Gate sequence to amplify amplitude errors of the R_{ZX} gate. (b) Echoed cross-resonance R_{ZX} pulse schedule of *ibmq_jakarta* qubits 1 and 3. The X pulses in the echo are shown in green on channel D1. The rotary tones and cross-resonance drives are shown in blue and brown, respectively. Channel U3 is a control channel that applies pulses to the control qubit at the frequency of the target qubit. (c) Target qubit population of standard measurements with a 4% amplitude error. (d) Probability of a state change in the target qubit obtained with restless measurements with a 4% amplitude error. The solid and dashed lines show measurements where the control qubit is initialized in $|0\rangle$ and $|1\rangle$, respectively. (e) The measured deviation angle $d\theta$ as a function of the added amplitude error. The average size of the error bars on the standard and restless data are 1.4 and 1.7 mrad, respectively. (f) Difference between the standard deviation angle $d\theta_S$ and the restless deviation angle $d\theta_R$ in (e).
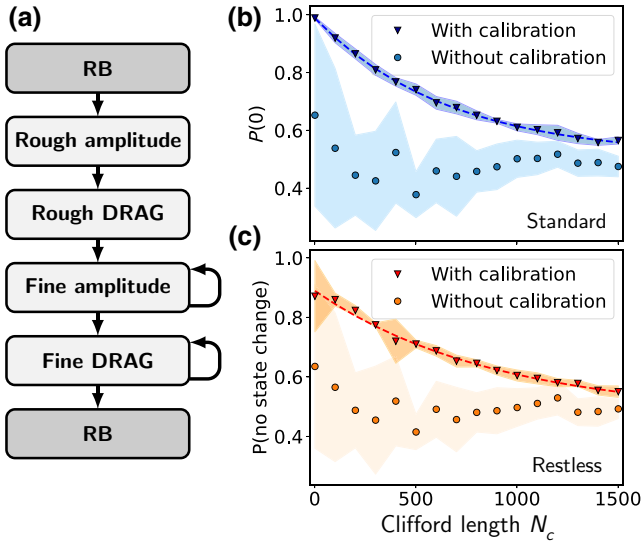
FIG. 8. Calibration of A and β of a $\sqrt{X}$ gate. (a) Schematic overview of the calibration experiments. Parameter scans yield rough values for A and β. Looped error-amplifying sequences are used as fine calibration experiments. Standard (b) and restless (c) RB done before (circles) and after (triangles) the calibration.

0.222 ns duration. First, we measure a Rabi oscillation by scanning A, which yields a rough estimate of the amplitude [23]. Next, we scan β using the experiment described in Sec. IV A, which yields a rough estimate of the DRAG parameter. We refine these rough estimates by looping the error-amplifying sequences described in Sec. IV B. Here, each experiment is repeated until the measured $d\theta$ is below a given tolerance or a maximum number of iterations is exceeded. Prior to and after the calibration we measure the quality of the $\sqrt{X}$ gate with RB. This workflow is shown in Fig. 8(a).

As an initial guess, we choose $A = 0.25$ and $\beta = 0$. With these values, both standard and restless RB show a low gate quality; see the light blue and orange circles in Figs. 8(b) and 8(c), respectively. The amplitude and DRAG parameter values obtained from the rough calibrations are starting points for the iterative fine calibration experiments. Both the standard and restless fine amplitude calibration experiments reach $d\theta \leq 1$ mrad tolerance after five iterations while the fine DRAG calibration experiments required eight iterations. The standard and restless calibration experiments yield amplitudes of $A_S = (9.486 \pm 0.004) \times 10^{-2}$ and $A_R = (9.512 \pm 0.004) \times 10^{-2}$ and DRAG parameters of $\beta_S = -0.39 \pm 0.03$ and $\beta_R = -0.29 \pm 0.03$, respectively. The backend reports $A = (9.501 + 0.080i) \times 10^{-2}$ and $\beta = -0.42$ as calibrated values. Standard and restless RB of the pulses we calibrated produced EPCs of $0.075\% \pm 0.006\%$ and $0.066\% \pm 0.013\%$, respectively; see the dark blue and red triangles in Figs. 8(b) and 8(c). The backend reported an

error per $\sqrt{X}$ gate of 0.037%. The total execution time on the quantum processor, which does not include data-transfer, queuing, and run-time compilation times, of the two RB and 15 calibration experiments was 187.0 and 11.6 s for the standard and restless experiments, respectively. Here, the 15 calibration experiments accounted for 94.6 and 2.3 s for standard and restless measurements, respectively.

V. PROCESS TOMOGRAPHY

Since RB is robust to SPAM errors, restless and standard measurements produce identical results. We now discuss restless process tomography measurements to characterize a quantum channel $\mathcal{E}$. Applying $\mathcal{E}$ on a density matrix ρ_j^{in} results in the output density matrix

$$\rho_j^{\text{out}} = \mathcal{E}(\rho_j^{\text{in}}) = \sum_{m,n=0}^{d^2-1} \chi_{mn} E_m \rho_j^{\text{in}} E_n^{\dagger}. \quad (4)$$

Here, the E_m form a basis of the $d \times d$ complex matrices where d is the dimension of the Hilbert space. Standard quantum process tomography reconstructs the matrix χ_{mn} describing $\mathcal{E}$ by preparing different input states ρ_j^{in} and measuring them in a complete basis [28–31]. By writing each ρ_j^{out} and ρ_j^{in} in a common basis ρ_k of density matrices, Eq. (4) becomes

$$c_{jk} = \sum_{mn} \chi_{mn} B_{mnjk}, \quad (5)$$

where $\rho_j^{\text{out}} = \sum_k c_{jk}\rho_k$ is determined with state tomography, and B_{mnjk} depends on ρ_j^{in}. Inverting Eq. (5) yields the process matrix χ that can be made physical with different methods [28,32,53]. A prerotation U_j^{pre} applied to the initial state $|0\rangle$ creates ρ_j^{in}. A complete input basis is formed for each qubit by choosing the gate set $\{I, X, H, SH\}$ as prerotations to prepare the eigenstates $\{Z_p, Z_m, X_p, Y_p\}$, respectively. Here, for example, Z_p and Z_m denote the eigenstates of the Z operator with positive and negative eigenvalues, respectively. Choosing postrotations U_i^{post} from $\{I, H, HS^{\dagger}\}$ allows us to measure along the Z, X, and Y axes, respectively.

The input state of each qubit in an ideal restless measurement is either $|0\rangle$ or $|1\rangle$. If the outcome of the previous measurement is $|1\rangle$, it is as if the prerotation is $U_j^{\text{pre}}X$; see Fig. 9. Therefore, in restless QPT, when the previous outcome was $|1\rangle$, the set of prerotations $\{I, X, H, SH\}$ is remapped to $\{X, I, HX, SHX\}$ that prepare the eigenstates $\{Z_m, Z_p, X_m, Y_m\}$, respectively. A postprocessing step is thus required to reassign the labels of the measured single shots to the set of eigenstates $\{Z_p, Z_m, X_p, X_m, Y_p, Y_m\}$; see, e.g., Fig. 10. We apply readout error mitigation to the resulting count dictionaries [54,55]. For one and two
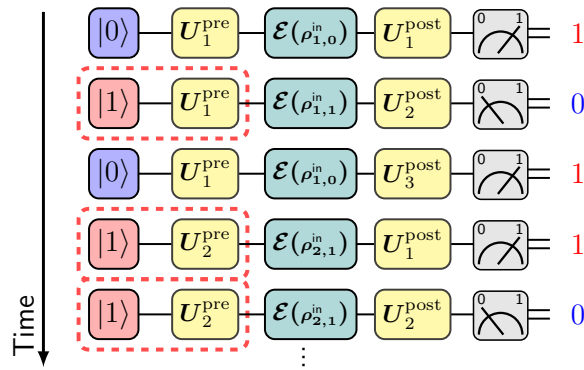
FIG. 9.   Illustration of the first five circuits of single-qubit restless QPT. Each circuit consists of a prerotation U_j^{pre}, the quantum process $\mathcal{E}$ to characterize, and a postrotation U_i^{post}. For the first circuit, the qubit is initialized in the ground state. If the qubit is measured in the excited state, the subsequent circuit starts with the qubit in state $|1\rangle$. In a postprocessing step these circuits are remapped to circuits with prerotation $U_j^{\mathrm{pre}}X$, indicated by the dashed red boxes.

qubits, this requires measuring two and four circuits to prepare each basis state. Note, however, that this readout error mitigation does not overcome any restless-related state preparation errors.

We benchmark the reconstruction process by performing standard and restless QPT of n consecutive Hadamard gates with n varying from 10 to 100 on *ibmq_sydney* qubits 3 and 5. Standard QPT measures fidelities of $97.6\% \pm 0.3\%$ and $82.8\% \pm 0.5\%$ (qubit 3) and $97.7\% \pm 0.2\%$ and $87.8\% \pm 2.2\%$ (qubit 5) for 10 to 100 Hadamards, respectively. We see in Figs. 11(a) and 11(b) that the fidelity $\mathcal{F}_R$ of the restless QPT is on average $6.0\% \pm 0.6\%$ and $3.9\% \pm$
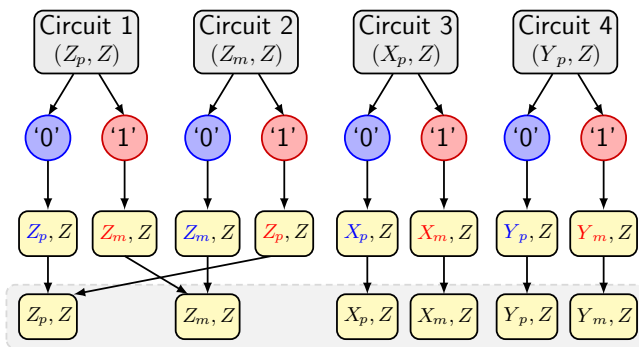

FIG. 11.   Standard and restless QPT of 10 to 100 Hadamard gates. The experiments are performed on *ibmq_sydney* qubits 3 (a),(c),(e),(g) and 5 (b),(d),(f),(h). Each fidelity is measured three times with 4096 shots; the markers show the average and the error bars the standard deviation. (a),(b) Standard (blue circles), restless fidelities (orange up triangles), and restless fidelities computed using the preparation-error-mitigated input states with p based on T_1 (purple down triangles). (c),(d) Difference between the purple down triangles and the blue circles. (e),(f) Restless preparation-error-mitigated fidelities based on a fit of the restless data to the standard QPT data (violet down triangles). (g),(h) Difference between the data points in (e) and (f), respectively.

FIG. 10.   Ideal restless input state reassignment for $U_i^{\mathrm{post}} = Z$. Since we time order the measured outcomes, we know the circuit that generated each shot (gray boxes) and the outcome of the previous measurement (circles). This allows us to reassign the measured outcome to the correct preparation basis (yellow boxes). Lastly, all outcomes are consolidated and assigned to the $\{Z_p, Z_m, X_p, X_m, Y_p, Y_m\}$ states.
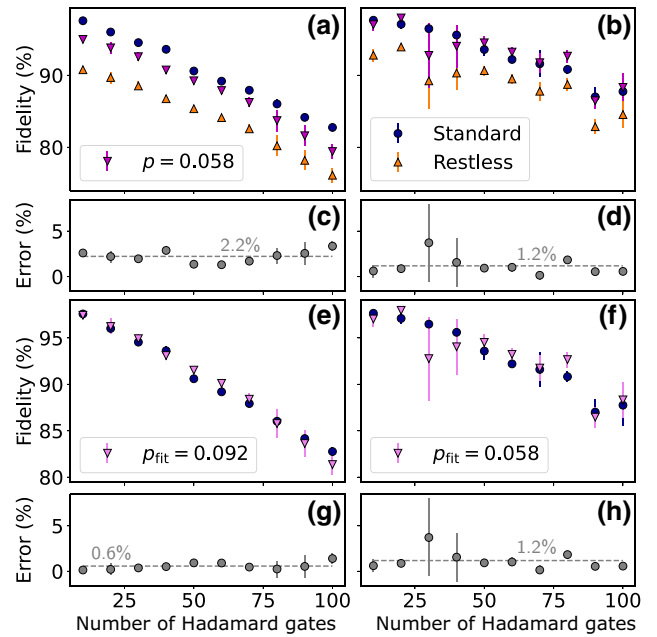
1.4% lower than standard measured fidelity $\mathcal{F}_S$, respectively; compare the orange triangles with the blue circles. This difference is independent of the process fidelity, which opens up the possibility of using restless QPT as a fast cost function for optimal control. This discrepancy is because measurement and T_1 may induce state preparation errors when the outcome $|1\rangle$ is measured.

A. Error mitigation

So far, we have assumed that the state after each readout is either $|0\rangle$ or $|1\rangle$ since the measurement pushes the qubit towards eigenstates of the Z operator [56] while increasing dephasing [57,58]. However, the finite qubit T_1 causes $|1\rangle \rightarrow |0\rangle$ jumps during the delay and the readout with probability p that we approximate by $p = 1 - \exp\left(-[\tau_{\mathrm{meas}} + \tau_{\mathrm{delay}}]/T_1\right)$. We therefore model the initial state following a $|1\rangle$ outcome by an amplitude damping channel $\mathcal{E}_{\mathrm{AD}}$ with strength p applied to $|1\rangle\langle 1|$, i.e., $\mathcal{E}_{\mathrm{AD}}(|1\rangle\langle 1|) = p\,|0\rangle\langle 0| + (1-p)\,|1\rangle\langle 1|$. To mitigate the errors in restless QPT shown in Figs. 11(a) and 11(b), we modify the preparation basis that now includes

the eight states

$$\rho_{j,0}^{\text{in}} = U_j^{\text{pre}} |0\rangle\langle 0| (U_j^{\text{pre}})^\dagger \quad (6)$$

and $\quad \rho_{j,1}^{\text{in}} = U_j^{\text{pre}}[p |0\rangle\langle 0| + (1-p) |1\rangle\langle 1|](U_j^{\text{pre}})^\dagger, \quad (7)$

where $j \in \{1, 2, 3, 4\}$; see the details in Appendix D. The decay probability is $p = 0.058$ for both qubits 3 and 5 since at the time the QPT data was taken they had a T_1 of 106.5 and 105.7 μs, respectively, while $\tau_{\text{meas}} = 5.4$ μs and $\tau_{\text{delay}} = 1$ μs. With the modified preparation basis in Eqs. (6) and (7), the error between the restless and standard fidelities is reduced to 2.2% ± 0.6% and 1.2% ± 1.0% on average for qubits 3 and 5, respectively; see Figs. 11(c) and 11(d) and the purple triangles in Figs. 11(a) and 11(b). This error is further reduced if we treat p in Eq. (7) as a fit parameter. We thus find the p_{fit} that minimizes the sum of squared errors between the restless and standard fidelities, i.e., $p_{\text{fit}} = \min_p \sum [\mathcal{F}_R(p) - \mathcal{F}_S]^2$, where the sum is carried out over each QPT measurement. This results in $p_{\text{fit}} = 0.092$ and $p_{\text{fit}} = 0.058$ for qubits 3 and 5, respectively; see Figs. 11(e) and 11(f). This further reduces the error between restless and standard QPT measurements to 0.6% ± 0.4% for qubit 3, on average; see Figs. 11(g) and 11(h). This shows that p suffices to describe the discrepancy between restless and standard QPT data. If the effect of the measurement process is well understood, we can compensate the T_1-induced errors using the restless preparation basis. The fluctuations in the data for qubit 5 suggest that restless QPT is more unstable than standard QPT. This could be explained by the higher sensitivity to measurement or T_1-induced errors since T_1 is known to fluctuate [59,60].

We further demonstrate two-qubit restless QPT of one to ten random SU(4) gates on qubits 3 and 5 of *ibmq_sydney*. Here, the ith two-qubit gate is decomposed into three CNOT gates and single-qubit gates [61]; see Fig. 12(a). The single-qubit gates depend on the three angles (α_i, β_i, γ_i) that we chose at random within the Weyl chamber [62–64]. We observe a high error of 6.0% ± 0.5%, on average, between $\mathcal{F}_R$ and $\mathcal{F}_S$ when $p = 0$; see the orange and blue markers in Fig. 12(b). However, when we compute the restless fidelities with the decay probabilities $p = \{0.041, 0.051\}$, based on the T_1 times of 151.0 μs for qubit 3 and 122.4 μs for qubit 5 at the time the QPT data was taken, the average deviation between the restless fidelities and the standard fidelities is reduced to 1.1% ± 0.8%; see Fig. 12(c). Errors of up to 3.2%, e.g., for ten random SU(4) gates, are still present, which we attribute to the higher sensitivity of restless QPT to SPAM errors.

We also run restless QPT on *ibmq_manila* and *ibmq_montreal*, and the data, presented in Appendix D, show a similar behavior. The T_1 and T_2 times and readout errors of all used qubits are listed in Table IV in Appendix C.
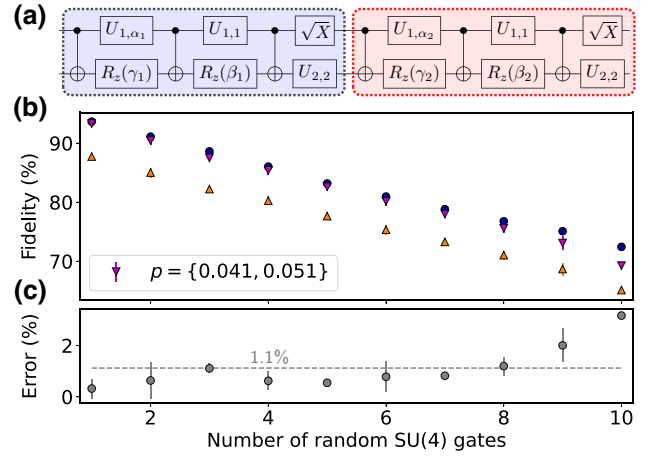

FIG. 12. Standard and restless QPT of one to ten random SU(4) gates. The experiments are performed on *ibmq_sydney* qubits 3 and 5. (a) Two SU(4) gates with angles (α_i, β_i, γ_i) chosen at random in the Weyl chamber. Here, $U_{n,m}$ and $U_{1,\alpha}$ correspond to $R_z(n\pi/2)\sqrt{X}R_z(m\pi/2)$ and $R_z(\pi/2)\sqrt{X}R_z(\alpha)$, respectively. (b) Standard QPT (blue circles), postprocessed restless QPT (orange triangles), and restless preparation basis QPT results (purple triangles) for qubits 3 and 5. Each fidelity is measured three times with 4096 shots. The T_1-induced decay probability is $p \approx 0.041$ and $p \approx 0.051$ for qubits 3 and 5, respectively. (c) Absolute deviation of the restless preparation basis QPT results from the standard QPT results.

B. Restless QPT speed-up

We compute the restless speed-up using Eq. (1). For single-qubit QPT with ten Hadamard gates and two-qubit QPT with one random SU(4) gate on *ibmq_sydney*, we obtain an average circuit duration of $\langle\tau_{\text{circ}}\rangle$ of 0.41 and 1.24 μs, respectively; see Table II. A restless repetition delay of 1 μs leads to a 38.7 and 34.1 times speed-up for single- and two-qubit QPT, respectively. On systems like *ibmq_montreal* with a default repetition delay of 50 μs and a restless repetition delay of 0.5 μs, we obtain a 9.8 and 8.3 times speed-up for single- and two-qubit QPT, respectively; see Appendix D.

VI. CONCLUSION

We have investigated restless calibration and characterization on cloud-based quantum computers. Turning active reset off and reducing the delay between the end of a measurement and the beginning of the next circuit creates a restless setting. Crucially, the restless measurements are now done with a dynamic repetition rate as opposed to a fixed repetition rate [23]. This enables randomized benchmarking with excellent agreement to standard measurements without discarding any data, as done in Ref. [23] that also limited the scalability of restless measurements.

We have also demonstrated restless qubit calibration of the amplitude and DRAG parameter of a single-qubit

TABLE II. Run-time breakdown on the quantum processor of one- and two-qubit QPT of ten Hadamard gates and one random SU(4) gate with $N_{shots} = 4096$. The single- and two-qubit *ibmq_sydney* QPT data were measured on November 2, 2021 and December 21, 2021, respectively.

Processor (restless)	τ_{meas} (μs)	τ_{reset}[a] (μs)	τ_{delay} (μs)	$\langle \tau_{circ} \rangle$ (μs)	$\tau^{(x)}$ (s)
Single-qubit QPT					
ibmq_sydney (✗)	5.4	4	250.0	0.41	12.77
ibmq_sydney (✓)	5.4	n.m.	1.0	0.41	0.33
ibmq_montreal (✗)	5.2	4	50.0	0.41	2.93
ibmq_montreal (✓)	5.2	n.m.	0.5	0.41	0.30
Two-qubit QPT					
ibmq_sydney (✗)	5.4	4	250.0	1.24	153.73
ibmq_sydney (✓)	5.4	n.m.	1.0	1.24	4.51
ibmq_montreal (✗)	5.2	4	50.0	1.64	35.89
ibmq_montreal (✓)	5.2	n.m.	0.5	1.64	4.33

[a]We assume $4\,\mu$s since the backends do not disclose the exact duration of the reset, which is typically between 3 and 5 μs.

pulse. Here, restless measurements yield a speed-up ranging from 9 to 38 times. When including the RB characterization, the qubit calibration is 16 times faster with restless measurements. These speed-ups depend on the quality of the active reset to which we compare. As active reset improves the default repetition, delay on the system will shorten, therefore lowering the speed-up. Restless measurements will nevertheless have the lowest run time on the quantum processor since they require the lowest number of operations. Restless measurements have the added benefit that they do not require active reset, therefore eliminating reset-related issues from fast characterization and calibration tasks. Importantly, the speed-ups that we measure do not take into account the classical run-time compilation and data transfer times that can be significant [7]. This shows that increasing the speed at which quantum systems are calibrated depends both on the quantum and the classical hardware. Here, we have focused on the quantum hardware.

Furthermore, we have demonstrated restless measurements of a two-qubit error amplifying gate sequence. Two-qubit experiments have the added complexity that the effect of the gate depends on the state of both qubits. The restless postprocessing must accommodate this by possibly separating the data into two series conditional on the state of the control qubit.

We have also shown that it is possible to perform QPT with restless measurements as long as the effect of the readout is well understood and the system is stable. Speeding up QPT becomes even more relevant as the system size increases [65]. This task may be complicated by any effect that the readout may have on the qubit [36,66]. We observed that restless QPT measured fidelities scale with

the number of gates, as expected even when state preparation errors are not mitigated. The 10 to 39 times speed-up afforded by restless QPT opens up the possibility to use it as a fast cost function for closed-loop optimal control [19,20] even if it does not exactly match the fidelity with standard measurements. By contrast to QPT, gate set tomography [67–70] is less vulnerable to state preparation and measurement errors. Future work may therefore explore whether gate set tomography can be performed with restless measurements and extend restless measurements to many-qubit protocols such as cycle benchmarking that measures the performance of parallel gate cycles and is robust to SPAM errors [71].

In conclusion, restless measurements offer a simple and fast alternative to reset-based measurements for calibration and characterization tasks [72]. This can increase the availability of cloud-based systems by reducing calibration and characterization time or increasing quality by running calibration more often. Restless measurements may also make it easier to handle the large calibration overhead required by Richardson error mitigation that calibrates several scaled versions of the same pulse set [73,74]. Finally, many error correcting protocols, such as the surface code [75,76], require repeated measurements of syndrome qubits. We envision that restless measurements may be used in error correcting codes to speed-up the error detection cycle—a key driver of the speed of fault-tolerant quantum computers—which may help obtain a quantum advantage at smaller problem sizes [77].

APPENDIX A: DYNAMIC REPETITION DELAY

To illustrate the impact of the repetition delay on restless measurements, we compute the state preparation and measurement fidelity as in Ref. [23]. We measure 20 circuits; the first ten are an I gate followed by a measurement and the second ten are an X gate followed by a measurement; see Fig. 13(a). With these circuits we measure two distinct errors. The first error occurs when circuit $k - 1$ measures $|0\rangle$ but the outcome of circuit k is $|1\rangle$ for an I gate or $|0\rangle$ for an X gate, i.e., $P_0(1|I) + P_0(0|X)$. The second error occurs when circuit $k - 1$ measures $|1\rangle$ but the
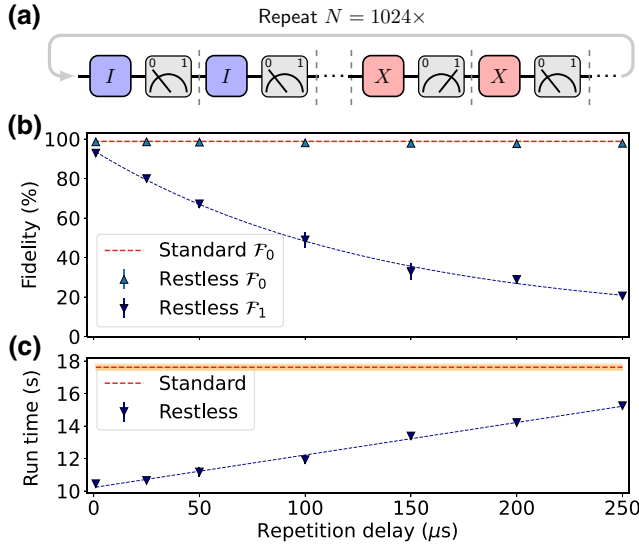
FIG. 13. Restless state preparation and measurement fidelities and total run times on *ibmq_sydney* qubit 5 for different repetition delays. (a) Twenty circuits with 10 identity and 10 X gates are measured. (b) Restless measurement fidelities $\mathcal{F}_0$ (blue up triangles) and $\mathcal{F}_1$ (dark blue dow triangles). Each point is the average of three individual measurements. The red dashed line shows the average standard fidelity $\mathcal{F}_0$ computed from the results of 3×7 interleaved jobs with active reset. (b) Mean reported total run times of the circuits in (b) in the standard (red dashed line) and restless (dark blue down triangles) settings. The shaded orange area and the error bars correspond to the standard deviation of the standard and restless run times, respectively.

outcome of circuit k is $|1\rangle$ for an X gate or $|0\rangle$ for an I gate, i.e., $P_1(0|I) + P_1(1|X)$. From these errors we compute the state preparation and measurement fidelities

$$\mathcal{F}_0 = 1 - \tfrac{1}{2}[P_0(1|I) + P_0(0|X)] \qquad \text{(A1)}$$

$$\text{and} \quad \mathcal{F}_1 = 1 - \tfrac{1}{2}[P_1(0|I) + P_1(1|X)]. \qquad \text{(A2)}$$

We evaluate these fidelities for different repetition delays ranging from 1 to 250 μs and with 1024 shots. At 1 μs we measure $\mathcal{F}_0 = 98.57\% \pm 0.03\%$ and $\mathcal{F}_1 = 92.86\% \pm 0.57\%$. We observe that $\mathcal{F}_0$ is independent of the repetition delay while $\mathcal{F}_1$ decays exponentially; see Fig. 13(b). This decay is caused by T_1, as confirmed by the exponential fit to $\mathcal{F}_1$ resulting in $T_{1,\text{fit}} = 131.5$ μs, in close agreement with the 134.1 μs T_1 reported by the backend. As a reference, we also run the circuits with an active reset and the default repetition delay of 250 μs interleaved and calculate $\mathcal{F}_0$. The resulting fidelities agree with $\mathcal{F}_0$ measured in the restless setting [see the orange dashed line in Fig. 13(b)], which is the average over 21 independent measurements.

IBM Quantum systems also report job execution times as the sum of the quantum processor time and the classical compile and data transfer times. The execution time when active reset is used with a repetition delay of 250 μs
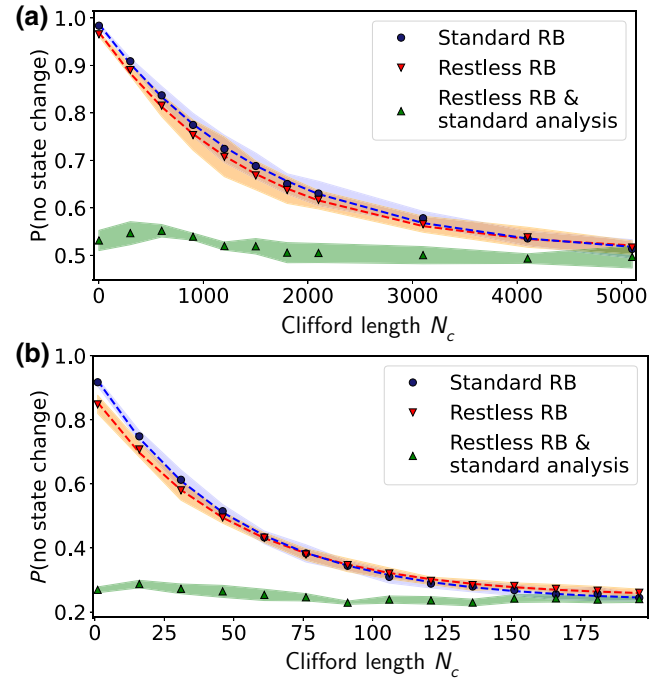

FIG. 14. Standard and restless RB on *ibmq_montreal*. (a) Single-qubit RB for qubit 0. (b) Two-qubit RB for qubits 1 and 2. Each marker indicates the mean value of ten Clifford sequences and the shaded area shows the standard deviation. The green triangles show restless data analyzed with the standard data processor.

is constant at 17.6 ± 0.2 s averaged over 21 independent jobs; see the dashed line in Fig. 13(c). For restless measurements, the execution time increases linearly as a function of the repetition delay. The measured slope is 0.02 s/μs, which corresponds to an extra $20 \times 1024 \times 10^{-6} \approx 0.02$ s per each extra microsecond of added delay, as expected from Eq. (1) and the 20 circuits each measured 1024 times.

APPENDIX B: ADDITIONAL RESTLESS RANDOMIZED BENCHMARKING DATA

Here, we show in Table III the fit parameter α and the EPC for each of the three RB measurements done on *ibmq_sydney* that were summarized in the main text. We also present additional restless and standard RB data acquired on *ibmq_montreal*. On *ibmq_montreal* standard measurements have a default 50 μs delay after a reset. We perform restless RB with a 0.5 μs delay after each measurement. Single-qubit RB on qubit 0 yields an EPC = $0.031\% \pm 0.001\%$ and EPC = $0.033\% \pm 0.001\%$ for three independent standard and restless RB experiments, respectively; see Fig. 14 and Table III.

Two-qubit RB is done on qubits 1 and 2 of *ibmq_montreal* for which we measure EPC = $1.502\% \pm 0.027\%$ and EPC = $1.495\% \pm 0.035\%$ for three independent standard and restless RB experiments, respectively; see

TABLE III.   Standard and restless RB fit data. Here $N_c^{\max}$ indicates the maximum number of Clifford gates in a RB experiment. The errors indicate one standard deviation.

Experiment	α (%)	EPC (%)	A	B
ibmq_sydney				
Qubit 13	99.945(1)	0.028(1)	0.493(4)	0.503(4)
Standard	99.946(1)	0.027(1)	0.494(6)	0.501(6)
$N_c^{\max} = 5101$	99.901(2)	0.050(1)	0.487(3)	0.505(3)
ibmq_sydney				
Qubit 13	99.945(2)	0.028(1)	0.475(6)	0.493(6)
Restless	99.941(2)	0.029(1)	0.463(5)	0.503(6)
$N_c^{\max} = 5101$	99.902(2)	0.049(1)	0.458(4)	0.496(3)
ibmq_sydney				
Qubits 8 & 11	97.745(42)	1.692(32)	0.669(4)	0.259(3)
Standard	97.709(38)	1.718(28)	0.678(4)	0.255(3)
$N_c^{\max} = 196$	97.735(42)	1.699(32)	0.663(4)	0.258(2)
ibmq_sydney				
Qubits 8 & 11	97.631(46)	1.777(34)	0.586(5)	0.248(2)
Restless	97.602(53)	1.799(40)	0.585(4)	0.251(2)
$N_c^{\max} = 196$	97.647(48)	1.765(36)	0.573(5)	0.256(2)
ibmq_montreal				
Qubit 0	99.931(1)	0.035(1)	0.486(3)	0.499(3)
Standard	99.941(2)	0.029(1)	0.494(6)	0.491(6)
$N_c^{\max} = 5101$	99.941(2)	0.030(1)	0.493(6)	0.492(6)
ibmq_montreal				
Qubit 0	99.932(2)	0.034(1)	0.464(5)	0.497(5)
Restless	99.932(3)	0.034(1)	0.461(6)	0.506(6)
$N_c^{\max} = 5101$	99.935(2)	0.033(1)	0.465(5)	0.501(5)
ibmq_montreal				
Qubits 1 & 2	98.021(36)	1.484(27)	0.703(4)	0.231(3)
Standard	97.994(36)	1.505(27)	0.695(4)	0.234(3)
$N_c^{\max} = 196$	97.976(37)	1.518(28)	0.693(5)	0.236(3)
ibmq_montreal				
Qubits 1 & 2	97.996(45)	1.503(34)	0.621(7)	0.249(3)
Restless	97.987(46)	1.510(34)	0.614(8)	0.252(2)
$N_c^{\max} = 196$	98.038(51)	1.472(38)	0.619(7)	0.247(3)

TABLE IV.   Summary of qubit decay, coherence times, and readout errors as reported by the backends.

Device	T_1 time (μs)	T_2 time (μs)	Readout error (%)
Single-qubit RB			
ibmq_sydney q13	134.5	156.3	1.70
ibmq_montreal q0	104.7	30.4	0.99
Two-qubit RB			
ibmq_sydney			
q8	105.4	173.8	3.74
q11	135.9	101.3	1.53
ibmq_montreal			
q1	102.9	23.2	1.66
q2	91.5	121.0	1.17
Single-qubit cal.			
ibmq_quito q1	58.3	131.5	1.88
ibmq_jakarta q1	116.9	21.9	1.96
ibmq_montreal q3	83.0	70.7	0.74
Two-qubit cal.			
ibmq_jakarta			
q1	131.1	25.5	2.06
q3	117.7	36.3	2.48
$\sqrt{X}$ calibration			
ibmq_bogota q2	105.2	176.2	1.91
Single-qubit QPT			
ibmq_sydney			
q3	106.5	98.8	1.87
q5	105.7	70.8	0.69
ibmq_montreal			
q13	89.3	76.3	0.98
q14	91.8	74.2	1.58
ibmq_manila			
q2	170.5	19.5	4.88
q3	172.9	65.8	1.69
Two-qubit QPT			
ibmq_sydney			
q3	151.0	100.3	1.93
q5	122.4	90.4	2.42
ibmq_montreal			
q13	56.8	30.6	2.22
q14	94.3	116.4	1.50
ibmq_manila			
q2	160.9	19.0	4.0
q3	178.7	54.3	2.6

Fig. 14(b). To demonstrate the importance of the restless data processor, we process the restless data with the standard data processing chain in which the measured outcomes are simply aggregated in count dictionaries. This results in the useless green curve in Figs. 14(a) and 14(b).

APPENDIX C: DEVICE PROPERTIES

We run the RB, calibration, and QPT experiments on different qubits of various quantum devices based on system availability. This also shows that restless measurements are reproducible across different backends. Since restless measurements are sensitive to finite T_1 times, we list the T_1 times of all qubits in Table IV. For completeness, we also include the T_2 times, as well as the readout errors, that were reported by the backend at the time of the respective experiment.

APPENDIX D: PROCESS TOMOGRAPHY

Here, we elaborate on the restless data processing for QPT. When the qubits are initialized to $|0\rangle$, the input density matrices are always $\rho_j^{\text{in}} = U_j^{\text{pre}} |0\rangle\langle 0| (U_j^{\text{pre}})^\dagger$. In an ideal restless measurement on n qubits the input density matrix is $\rho_{j,x}^{\text{in}} = U_j^{\text{pre}} |x\rangle\langle x| (U_j^{\text{pre}})^\dagger$, where $x \in \{0,1\}^n$.
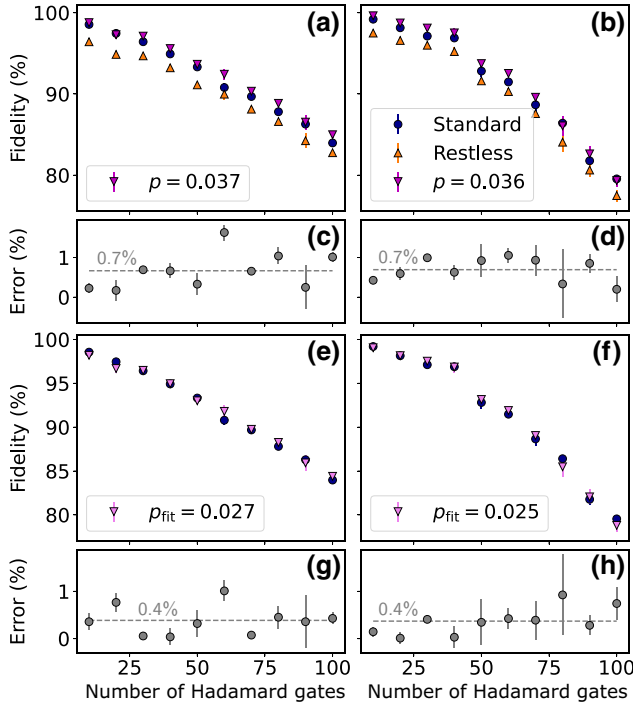
FIG. 15. Single-qubit QPT on qubits 2 (a),(c),(e),(g) and 3 (b),(d),(f),(h) of *ibmq_manila*. Panels (c) and (d) show the difference between the standard QPT data and the restless QPT data with p obtained from T_1 times reported by the backend of 170.5 and 172.9 μs for qubits 2 and 3, respectively. Panels (e) and (f) show the best restless measured fidelity when treating p as a fit parameter and panels (g) and (h) show the deviation $|\mathcal{F}_R(p_{\text{fit}}) - \mathcal{F}_S|$.

However, in practice the measurement and the delay between the measurement and the next U_j^{pre} induce errors that we model by an amplitude damping channel $\mathcal{E}_{\text{AD}}$. In the single-qubit case the input states are given by Eqs. (6) and (7) of the main text that trivially generalize to n
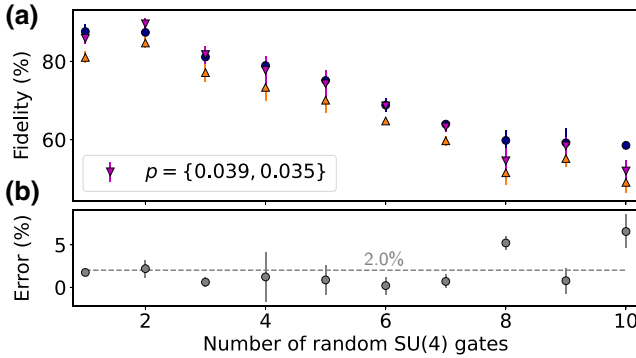

FIG. 16. (a) QPT on random SU(4) gates between qubits 2 and 3 of *ibmq_manila*. The purple down triangles show the restless fidelity with p based on T_1 times reported by the backend of 160.9 and 178.7 μs for qubits 2 and 3, respectively. (b) The difference $|\mathcal{F}_R(p) - \mathcal{F}_S|$ between the fidelities measured with restless and active reset.
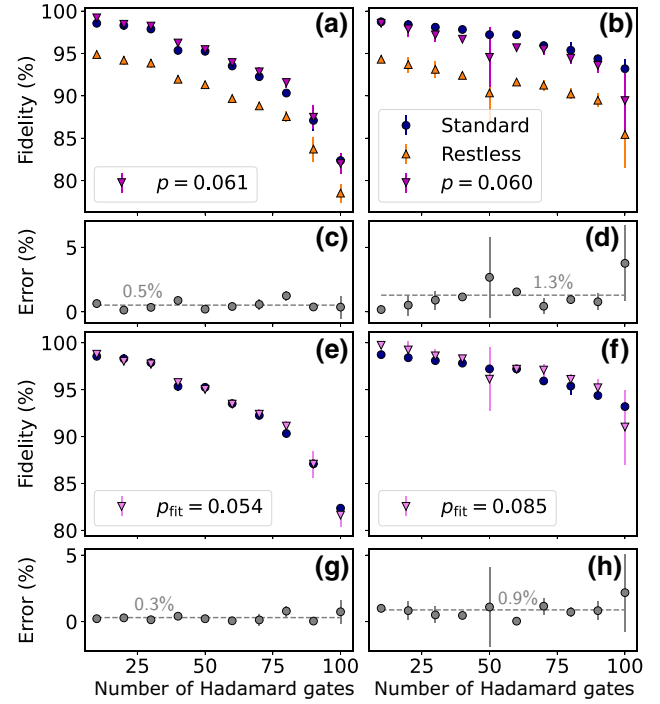

FIG. 17. Single-qubit QPT on qubits 13 (a),(c),(e),(g) and 14 (b),(d),(f),(h) of *ibmq_montreal*. Panels (c) and (d) show the difference between the standard QPT data and the restless QPT data with p obtained from T_1 times reported by the backend of 89.3 and 91.8 μs for qubits 13 and 14, respectively. Panels (e) and (f) show the best restless measured fidelity when treating p as a fit parameter and panels (g) and (h) show the deviation $|\mathcal{F}_R(p_{\text{fit}}) - \mathcal{F}_S|$.

qubits. This results in a total of $4^n \times 2^n$ possible input states when only 4^n preparation rotations U_j^{pre} are done. Taking into account the three measurement bases, there is a total of $4^n \times 2^n \times 3^n$ combinations of input states and measurement basis. However, restless QPT only executes $4^n \times 3^n$ circuits, as does standard QPT. The restless QPT data processor must therefore remap each measured shot to one of the $4^n \times 2^n \times 3^n$ combinations. To postprocess restless QPT data, we require the memory of each circuit, as discussed in Sec. II A of the main text. Once again, we time order all the measurement outcomes. If, for $(U_j^{\text{pre}}, U_i^{\text{post}})$, the previous measurement outcome was $|0\rangle$, we attribute the corresponding measurement to the input state $U_j^{\text{pre}} |0\rangle\langle 0| (U_j^{\text{pre}})^\dagger$ and postrotation U_i^{post}. However, if the previous measurement outcome was $|1\rangle$, we attribute the measurement to the input state $U_j^{\text{pre}}[p\,|0\rangle\langle 0| - (1-p)\,|1\rangle\langle 1|](U_j^{\text{pre}})^\dagger$ and postrotation U_i^{post}. This reasoning extends trivially to the multiqubit case. Since we now know the input state and measurement basis of each shot, we can build up count dictionaries for each of the $4^n \times 2^n \times 3^n$ possible combinations. The remainder of the analysis follows the standard QPT work flow.
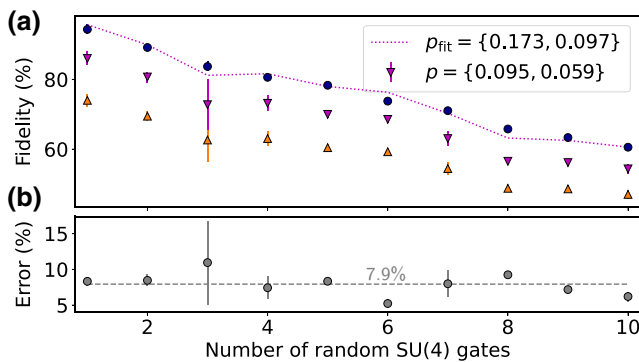
FIG. 18. (a) QPT on random SU(4) gates between qubits 13 and 14 of *ibmq_montreal*. The purple down triangles show the restless fidelity with p based on T_1 times reported by the backend of 56.8 and 94.3 μs for qubits 13 and 14, respectively. The dotted purple line indicates the restless measured fidelities when treating the decay probabilities p as fit parameters. (b) The difference $|\mathcal{F}_R(p) - \mathcal{F}_S|$ between the fidelities measured with restless and active reset. The deviation of, on average, 7.9% $\pm$ 1.3% is reduced to $\langle|\mathcal{F}_R(p_{\text{fit}}) - \mathcal{F}_S|\rangle = 1.3\% \pm 1.3\%$ for $p_{\text{fit}} = \{0.173, 0.097\}$.

1. Additional process tomography data

In addition to the data presented in the main text we also run standard and restless QPT on *ibmq_manila* (see Figs. 15 and 16) and *ibmq_montreal* (see Figs. 17 and 18). We characterized an even sequence of Hadamard gates, from 10 to 100, and a sequence of random CNOT decomposed SU(4) gates from one to ten. We run each QPT measurement with 4096 shots and each point is the average of three individual measurements with the standard deviation shown as error bars. Readout error mitigation is used. In Figs. 15 to 18 the blue circles indicate standard QPT measurements, the orange up triangles indicate restless QPT measurements by reassigning the shots to the basis $\{Z_m, Z_p, X_m, X_p, Y_m, Y_p\}$, and the purple down triangles show the same data but processed with the restless preparation basis corresponding to Eqs. (6) and (7) in the main text.

As in the main text, we observe that the restless QPT data analyzed under the assumption that restless measurements are ideal, i.e., when the previous outcome was $|1\rangle$, the initial state is $|1\rangle$, underestimate the gate fidelity. Furthermore, we observe that a finite p obtained from T_1, measurement, and delay times mitigates state preparation errors when using Eqs. 6 and (7) of the main text as input states. Furthermore, a few restless QPT measurements are biased by large outliers. The exact source of these outliers is unknown but could be due to measurement or T_1-related variations.

[1] E. Farhi, J. Goldstone, and S. Gutmann, A quantum approximate optimization algorithm, arXiv:1411.4028 (2014).

[2] J. Biamonte, P. Wittek, N. Pancotti, P. Rebentrost, N. Wiebe, and S. Lloyd, Quantum machine learning, Nature **549**, 195 (2017).

[3] N. Moll, P. Barkoutsos, L. S. Bishop, J. M. Chow, A. Cross, D. J. Egger, S. Filipp, A. Fuhrer, J. M. Gambetta, and M. Ganzhorn *et al.*, Quantum optimization using variational algorithms on near-term quantum devices, Quantum Sci. Technol. **3**, 030503 (2018).

[4] A. Kandala, K. Temme, A. D. Corcoles, A. Mezzacapo, J. M. Chow, and J. M. Gambetta, Error mitigation extends the computational reach of a noisy quantum processor, Nature **567**, 491 (2018).

[5] L. Braine, D. J. Egger, J. Glick, and S. Woerner, Quantum algorithms for mixed binary optimization applied to transaction settlement, IEEE Trans. Quantum Eng. **2**, 1 (2021).

[6] D. J. Egger, C. Gambella, J. Marecek, S. McFaddin, M. Mevissen, R. Raymond, A. Simonetto, S. Woerner, and E. Yndurain, Quantum computing for finance: State-of-the-art and future prospects, IEEE Trans. Quantum Eng. **1**, 1 (2020).

[7] A. Wack, H. Paik, A. Javadi-Abhari, P. Jurcevic, I. Faro, J. M. Gambetta, and B. R. Johnson, Quality, speed, and scale: Three key attributes to measure the performance of near-term quantum computers, arXiv:2110.14108 [quant-ph] (2021).

[8] A. W. Cross, L. S. Bishop, S. Sheldon, P. D. Nation, and J. M. Gambetta, Validating quantum computers using randomized model circuits, Phys. Rev. A **100**, 032328 (2019).

[9] P. Jurcevic, A. Javadi-Abhari, L. S. Bishop, I. Lauer, D. F. Bogorin, M. Brink, L. Capelluto, O. Günlük, T. Itoko, and N. Kanazawa *et al.*, Demonstration of quantum volume 64 on a superconducting quantum computing system, Quantum Sci. Technol. **6**, 025020 (2021).

[10] F. Motzoi, J. M. Gambetta, P. Rebentrost, and F. K. Wilhelm, Simple Pulses for Elimination of Leakage in Weakly Nonlinear Qubits, Phys. Rev. Lett. **103**, 110501 (2009).

[11] S. Sheldon, L. S. Bishop, E. Magesan, S. Filipp, J. M. Chow, and J. M. Gambetta, Characterizing errors on qubit operations via iterative randomized benchmarking, Phys. Rev. A **93**, 012301 (2016).

[12] S. J. Glaser, U. Boscain, T. Calarco, C. P. Koch, W. Köckenberger, R. Kosloff, I. Kuprov, B. Luy, S. Schirmer, and T. Schulte-Herbrüggen *et al.*, Training Schrödinger's cat: Quantum optimal control, Eur. Phys. J. D **69**, 279 (2015).

[13] R. Schutjens, F. Abu Dagga, D. J. Egger, and F. K. Wilhelm, Single-qubit gates in frequency-crowded transmon systems, Phys. Rev. A **88**, 052330 (2013).

[14] R. W. Heeres, P. Reinhold, N. Ofek, L. Frunzio, L. Jiang, M. H. Devoret, and R. J. Schoelkopf, Implementing a universal gate set on a logical qubit encoded in an oscillator, Nat. Commun. **8**, 94 (2017).

[15] M. Abdelhafez, B. Baker, A. Gyenis, P. Mundada, A. A. Houck, D. Schuster, and J. Koch, Universal gates for protected superconducting qubits using optimal control, Phys. Rev. A **101**, 022321 (2020).

[16] D. J. Egger and F. K. Wilhelm, Optimized controlled-Z gates for two superconducting qubits coupled through a resonator, Supercond. Sci. Technol. **27**, 014001 (2013).

[17] S. Kirchhoff, T. Keßler, P. J. Liebermann, E. Assémat, S. Machnes, F. Motzoi, and F. K. Wilhelm, Optimized cross-resonance gate for coupled transmon systems, Phys. Rev. A **97**, 042348 (2018).

[18] M. Werninghaus, D. J. Egger, F. Roy, S. Machnes, F. K. Wilhelm, and S. Filipp, Leakage reduction in fast superconducting qubit gates via optimal control, Npj Quantum Inf. **7**, 14 (2021).

[19] J. Kelly, R. Barends, B. Campbell, Y. Chen, Z. Chen, B. Chiaro, A. Dunsworth, A. G. Fowler, I.-C. Hoi, and E. Jeffrey *et al.*, Optimal Quantum Control Using Randomized Benchmarking, Phys. Rev. Lett. **112**, 240504 (2014).

[20] D. J. Egger and F. K. Wilhelm, Adaptive Hybrid Optimal Quantum Control for Imprecisely Characterized Systems, Phys. Rev. Lett. **112**, 240503 (2014).

[21] S. Machnes, E. Assémat, D. Tannor, and F. K. Wilhelm, Tunable, Flexible, and Efficient Optimization of Control Pulses for Practical Qubits, Phys. Rev. Lett. **120**, 150401 (2018).

[22] A. M. Rol, C. C. Bultink, T. E. O'Brien, S. R. de Jong, T. Lukas S., X. Fu, F. Luthi, R. F. L. Vermeulen, and J. C. de Sterke *et al.*, Restless Tuneup of High-Fidelity Qubit Gates, Phys. Rev. Appl. **7**, 041001 (2017).

[23] M. Werninghaus, D. J. Egger, and S. Filipp, High-Speed Calibration and Characterization of Superconducting Quantum Processors without Qubit Reset, PRX Quantum **2**, 020324 (2021).

[24] E. Magesan, J. M. Gambetta, and J. Emerson, Scalable and Robust Randomized Benchmarking of Quantum Processes, Phys. Rev. Lett. **106**, 180504 (2011).

[25] E. Magesan, J. M. Gambetta, B. R. Johnson, C. A. Ryan, J. M. Chow, S. T. Merkel, M. P. da Silva, G. A. Keefe, and M. B. Rothwell *et al.*, Efficient Measurement of Quantum Gate Error by Interleaved Randomized Benchmarking, Phys. Rev. Lett. **109**, 080505 (2012).

[26] A. D. Córcoles, J. M. Gambetta, J. M. Chow, J. A. Smolin, M. Ware, J. Strand, B. L. T. Plourde, and M. Steffen, Process verification of two-qubit quantum gates by randomized benchmarking, Phys. Rev. A **87**, 030301 (2013).

[27] N. Wittler, F. Roy, K. Pack, M. Werninghaus, A. S. Roy, D. J. Egger, S. Filipp, F. K. Wilhelm, and S. Machnes, Integrated Tool Set for Control, Calibration, and Characterization of Quantum Devices Applied to Superconducting Qubits, Phys. Rev. Appl. **15**, 034080 (2021).

[28] J. L. O'Brien, G. J. Pryde, A. Gilchrist, D. F. V. James, N. K. Langford, T. C. Ralph, and A. G. White, Quantum Process Tomography of a Controlled-NOT Gate, Phys. Rev. Lett. **93**, 080502 (2004).

[29] M. Mohseni, A. T. Rezakhani, and D. A. Lidar, Quantum-process tomography: Resource analysis of different strategies, Phys. Rev. A **77**, 032322 (2008).

[30] R. C. Bialczak, M. Ansmann, M. Hofheinz, E. Lucero, M. Neeley, A. D. O'Connell, D. Sank, H. Wang, J. Wenner, and M. Steffen *et al.*, Quantum process tomography of a universal entangling gate implemented with Josephson phase qubits, Nat. Phys. **6**, 409 (2010).

[31] M. A. Nielsen and I. L. Chuang, *Quantum Computation and Quantum Information: 10th Anniversary Edition* (Cambridge University Press, New York, 2010).

[32] M. Pechal, G. Salis, M. Ganzhorn, D. J. Egger, M. Werninghaus, and S. Filipp, Characterization and tomography of a hidden qubit, Phys. Rev. X **11**, 041032 (2021).

[33] N. Earnest, C. Tornow, and D. J. Egger, Pulse-efficient circuit transpilation for quantum applications on cross-resonance-based hardware, Phys. Rev. Res. **3**, 043088 (2021).

[34] E. O. Kiktenko, D. O. Norkin, and A. K. Fedorov, Confidence polytopes for quantum process tomography, New J. Phys. **23**, 123022 (2021).

[35] M. Devoret and R. J. Schoelkopf, Superconducting circuits for quantum information: An outlook, Science **339**, 1169 (2013).

[36] P. Krantz, M. Kjaergaard, F. Yan, T. P. Orlando, S. Gustavsson, and W. D. Oliver, A quantum engineer's guide to superconducting qubits, Appl. Phys. Rev. **6**, 021318 (2019).

[37] A. Blais, A. L. Grimsmo, S. M. Girvin, and A. Wallraff, Circuit quantum electrodynamics, Rev. Mod. Phys. **93**, 025005 (2021).

[38] C. Rigetti, J. M. Gambetta, S. Poletto, B. L. T. Plourde, J. M. Chow, A. D. Córcoles, J. A. Smolin, S. T. Merkel, J. R. Rozen, and G. A. Keefe *et al.*, Superconducting qubit in a waveguide cavity with a coherence time approaching 0.1 ms, Phys. Rev. B **86**, 100506 (2012).

[39] A. P. M. Place, L. V. H. Rodgers, P. Mundada, B. M. Smitham, M. Fitzpatrick, Z. Leng, A. Premkumar, J. Bryon, A. Vrajitoarea, and S. Sussman *et al.*, New material platform for superconducting transmon qubits with coherence times exceeding 0.3 milliseconds, Nat. Commun. **12**, 1779 (2021).

[40] D. Ristè, J. G. van Leeuwen, H.-S. Ku, K. W. Lehnert, and L. DiCarlo, Initialization by Measurement of a Superconducting Quantum Bit Circuit, Phys. Rev. Lett. **109**, 050507 (2012).

[41] L. C. G. Govia and F. K. Wilhelm, Unitary-Feedback-Improved Qubit Initialization in the Dispersive Regime, Phys. Rev. Appl. **4**, 054001 (2015).

[42] K. Geerlings, Z. Leghtas, I. M. Pop, S. Shankar, L. Frunzio, R. J. Schoelkopf, M. Mirrahimi, and M. H. Devoret, Demonstrating a Driven Reset Protocol for a Superconducting Qubit, Phys. Rev. Lett. **110**, 120501 (2013).

[43] P. Magnard, P. Kurpiers, B. Royer, T. Walter, J.-C. Besse, S. Gasparinetti, M. Pechal, J. Heinsoo, S. Storz, A. Blais, and A. Wallraff, Fast and Unconditional All-Microwave Reset of a Superconducting Qubit, Phys. Rev. Lett. **121**, 060502 (2018).

[44] D. J. Egger, M. Werninghaus, M. Ganzhorn, G. Salis, A. Fuhrer, P. Müller, and S. Filipp, Pulsed Reset Protocol for Fixed-Frequency Superconducting Qubits, Phys. Rev. Appl. **10**, 044030 (2018).

[45] A. D. Córcoles, M. Takita, K. Inoue, S. Lekuch, Z. K. Minev, J. M. Chow, and J. M. Gambetta, Exploiting Dynamic Quantum Circuits in a Quantum Algorithm with Superconducting Qubits, Phys. Rev. Lett. **127**, 100501 (2021).

[46] T. Alexander, N. Kanazawa, D. J. Egger, L. Capelluto, C. J. Wood, A. Javadi-Abhari, and D. C. McKay, Qiskit pulse: Programming quantum computers through the cloud with pulses, Quantum Sci. Technol. **5**, 044006 (2020).

[47] Qiskit Experiments, https://github.com/Qiskit/qiskit-experiments.

[48] D. C. McKay, C. J. Wood, S. Sheldon, J. M. Chow, and J. M. Gambetta, Efficient *Z* gates for quantum computing, Phys. Rev. A **96,** 022330 (2017).

[49] J. M. Gambetta, F. Motzoi, S. T. Merkel, and F. K. Wilhelm, Analytic control methods for high-fidelity unitary operations in a weakly nonlinear oscillator, Phys. Rev. A **83,** 012308 (2011).

[50] Z. Chen, J. Kelly, C. Quintana, R. Barends, B. Campbell, Y. Chen, B. Chiaro, A. Dunsworth, and A. G. Fowler *et al.*, Measuring and Suppressing Quantum State Leakage in a Superconducting Qubit, Phys. Rev. Lett. **116,** 020501 (2016).

[51] S. Sheldon, E. Magesan, J. M. Chow, and J. M. Gambetta, Procedure for systematically tuning up cross-talk in the cross-resonance gate, Phys. Rev. A **93,** 060302 (2016).

[52] N. Sundaresan, I. Lauer, E. Pritchett, E. Magesan, P. Jurcevic, and J. M. Gambetta, Reducing Unitary and Spectator Errors in Cross Resonance with Optimized Rotary Echoes, PRX Quantum **1,** 020318 (2020).

[53] J. A. Smolin, J. M. Gambetta, and G. Smith, Efficient Method for Computing the Maximum-Likelihood Quantum State from Measurements with Additive Gaussian Noise, Phys. Rev. Lett. **108,** 070502 (2012).

[54] S. Bravyi, S. Sheldon, A. Kandala, D. C. McKay, and J. M. Gambetta, Mitigating measurement errors in multiqubit experiments, Phys. Rev. A **103,** 042605 (2021).

[55] G. S. Barron and C. J. Wood, Measurement error mitigation for variational quantum algorithms, arXiv:2010.08520 [quant-ph] (2020).

[56] J. Gambetta, A. Blais, M. Boissonneault, A. A. Houck, D. I. Schuster, and S. M. Girvin, Quantum trajectory approach to circuit QED: Quantum jumps and the Zeno effect, Phys. Rev. A **77,** 012112 (2008).

[57] D. I. Schuster, A. Wallraff, A. Blais, L. Frunzio, R.-Z. Huang, J. Majer, S. M. Girvin, and R. J. Schoelkopf, 'AC Stark Shift and Dephasing of a Superconducting Qubit Strongly Coupled to a Cavity Field, Phys. Rev. Lett. **94,** 123602 (2005).

[58] J. Gambetta, A. Blais, D. I. Schuster, A. Wallraff, L. Frunzio, J. Majer, M. H. Devoret, S. M. Girvin, and R. J. Schoelkopf, 'Qubit-photon interactions in a cavity: Measurement-induced dephasing and number splitting, Phys. Rev. A **74,** 042318 (2006).

[59] P. V. Klimov, J. Kelly, Z. Chen, M. Neeley, A. Megrant, B. Burkett, R. Barends, K. Arya, B. Chiaro, and Y. Chen *et al.*, Fluctuations of Energy-Relaxation Times in Superconducting Qubits, Phys. Rev. Lett. **121,** 090502 (2018).

[60] M. Carroll, S. Rosenblatt, P. Jurcevic, I. Lauer, and A. Kandala, Dynamics of superconducting qubit relaxation times, arXiv:2105.15201 [quant-ph] (2021).

[61] G. Vidal and C. M. Dawson, Universal quantum circuit for two-qubit transformations with three controlled-NOT gates, Phys. Rev. A **69,** 010301 (2004).

[62] J. Zhang, J. Vala, S. Sastry, and B. K. Whaley, Geometric theory of nonlocal two-qubit operations, Phys. Rev. A **67,** 042313 (2003).

[63] N. Khaneja and S. Glaser, Cartan decomposition of $SU(2^n)$ and control of spin systems, Chem. Phys. **267,** 11 (2001).

[64] B. Drury and P. Love, Constructive quantum shannon decomposition from cartan involutions, J. Phys. A: Math. Theor. **41,** 395305 (2008).

[65] A. Galda, M. Cubeddu, N. Kanazawa, P. Narang, and N. Earnest-Noble, Implementing a ternary decomposition of the Toffoli gate on fixed-frequency transmon qutrits, arXiv:2109.00558 [quant-ph] (2021).

[66] P. Goy, J.-M. Raimond, M. Gross, and S. Haroche, Observation of Cavity-Enhanced Single-Atom Spontaneous Emission, Phys. Rev. Lett. **50,** 1903 (1983).

[67] S. T. Merkel, J. M. Gambetta, J. A. Smolin, S. Poletto, A. D. Córcoles, B. R. Johnson, C. A. Ryan, and M. Steffen, Self-consistent quantum process tomography, Phys. Rev. A **87,** 062119 (2013).

[68] R. Blume-Kohout, J. K. Gamble, E. Nielsen, J. Mizrahi, J. D. Sterk, and P. Maunz, Robust, self-consistent, closed-form tomography of quantum logic gates on a trapped ion qubit, arXiv:1310.4492 [quant-ph] (2013).

[69] D. Greenbaum, Introduction to quantum gate set tomography, arXiv:1509.02921 [quant-ph] (2015).

[70] R. Blume-Kohout, J. K. Gamble, E. Nielsen, K. Rudinger, J. Mizrahi, K. Fortier, and P. Maunz, Demonstration of qubit operations below a rigorous fault tolerance threshold with gate set tomography, Nat. Commun. **8,** 14485 (2017).

[71] A. Erhard, J. J. Wallman, L. Postler, M. Meth, R. Stricker, E. A. Martinez, P. Schindler, T. Monz, J. Emerson, and R. Blatt, Characterizing large-scale quantum computers via cycle benchmarking, Nat. Commun. **10,** 5347 (2019).

[72] M. Ganzhorn, G. Salis, D. J. Egger, A. Fuhrer, M. Mergenthaler, C. Müller, P. Müller, S. Paredes, M. Pechal, M. Werninghaus, and S. Filipp, Benchmarking the noise sensitivity of different parametric two-qubit gates in a single superconducting quantum computing platform, Phys. Rev. Res. **2,** 033447 (2020).

[73] K. Temme, S. Bravyi, and J. M. Gambetta, Error Mitigation for Short-Depth Quantum Circuits, Phys. Rev. Lett. **119,** 180509 (2017).

[74] A. Kandala, K. Temme, A. D. Córcoles, A. Mezzacapo, J. M. Chow, and J. M. Gambetta, Error mitigation extends the computational reach of a noisy quantum processor, Nature **567,** 491 (2019).

[75] A. G. Fowler, M. Mariantoni, J. M. Martinis, and A. N. Cleland, Surface codes: Towards practical large-scale quantum computation, Phys. Rev. A **86,** 032324 (2012).

[76] C. Chamberland, G. Zhu, T. J. Yoder, J. B. Hertzberg, and A. W. Cross, Topological and subsystem codes on low-degree graphs with flag qubits, Phys. Rev. X **10,** 011022 (2020).

[77] S. Chakrabarti, R. Krishnakumar, G. Mazzola, N. Stamatopoulos, S. Woerner, and W. J. Zeng, A threshold for quantum advantage in derivative pricing, Quantum **5,** 463 (2021).

[78] https://www.ibm.com/legal/copytrade.